Novel Detection Scheme for Temporal and Spectral X-Ray Optical Analysis: Study of Triple-Cation Perovskites

Christina Ossig,[1,2] Christian Strelow,[3] Jan Flügge,[3] Svenja Patjens,[1,3] Jan Garrevoet,[4] Kathryn Spiers,[4] Jackson L. Barp Jr.,[1,2] Johannes Hagemann,[1] Frank Seiboth,[1] Michele De Bastiani,[5] Erkan Aydin,[5,6] Furkan H. Isikgor,[5] Stefaan De Wolf,[5] Gerald Falkenberg,[4] Alf Mews,[3] Christian G. Schroer,[1,2,7] Tobias Kipp,[3] and Michael E. Stuckelberger[1,*]

[1] *Center for X-Ray and Nano Science (CXNS), Deutsches Elektronen-Synchrotron DESY, Notkestrasse 85, Hamburg 22607, Germany*

[2] *Department of Physics, Universität Hamburg, Notkestrasse 9-11, Hamburg 22607, Germany*

[3] *Institut für Physikalische Chemie, Universität Hamburg, Grindelallee 117, Hamburg 20146, Germany*

[4] *Deutsches Elektronen-Synchrotron DESY, Notkestrasse 85, Hamburg 22607, Germany*

[5] *KAUST Solar Center (KSC), Physical Sciences and Engineering Division (PSE), King Abdullah University of Science and Technology (KAUST), Thuwal 23955-6900, Kingdom of Saudi Arabia*

[6] *Department of Chemistry, Ludwig-Maximilians-Universität (LMU), Butenandtstraße 11 (E), Munich 81377, Germany*

[7] *Helmholtz Imaging, Deutsches Elektronen-Synchrotron DESY, Notkestrasse 85, Hamburg 22607, Germany*

(Received 28 July 2023; revised 17 April 2024; accepted 4 June 2024; published 27 June 2024)

Multimodal x-ray microscopy is key to assessing the property-functionality relationships of semiconductor devices with the utmost sensitivity and spatial resolution. Here, we report on a novel setup—the "Analyzer of X-ray excited Optical Luminescence Offering Temporal and spectraL resolution" (AXOLOTL)—and demonstrate its use by investigating a series of triple-cation mixed-halide perovskite solar cells (PSCs) with varying Cs content. These PSCs exhibit spatially varying performance and are thus ideally probed by multimodal x-ray microscopy to elucidate the origin of the performance variations. Specifically, our nanoscale characterization of the wrinkled perovskite photoabsorber unveils a segregation of I and Br, which is accompanied by a narrowed band gap and an increased charge-carrier lifetime in thick absorber areas. Overall, we demonstrate with this technique the spatial correlation of compositional inhomogeneities, topography, electrical performance, and optical performance, which is of highest interest for identifying loss mechanisms at the nanoscale in high-performance electronic device development, including solar cells.

DOI: 10.1103/PRXEnergy.3.023011

I. INTRODUCTION

In recent years, synchrotron-based hard x-ray raster-scanning microscopy setups have become invaluable tools to evaluate, with high spatial resolution, the composition and performance of semiconductor structures [1–4] and, especially, solar cells [5–8], as high-energy x rays allow the penetration of a full solar-cell stack.

To evaluate the local composition, x-ray fluorescence (XRF) is typically used, where a core electron is excited by absorbing an x-ray photon and the resulting core hole is filled by a higher-level electron under the emission of an XRF photon of element-specific energy. The tunable x-ray-beam energy at synchrotron beam lines allows us to choose the excitation energy such that the measurement is highly selective to the elements of interest.

To evaluate the local electrical performance with an x-ray probe, x-ray-beam-induced current (XBIC) [6,9] and voltage (XBIV) [10] measurements are performed. When charge carriers, locally excited by a focused hard x-ray beam, are collected or their potential is measured, lock-in amplification is often used to improve the signal-to-noise ratio [11]. Compared to laser-beam-induced current (LBIC) measurements [12,13], only a fraction of the

*Contact author: michael.stuckelberger@desy.de

incident photons is absorbed during XBIC measurements. However, these high-energy photons generate a cascade of excitations [14], where at the end of the thermalization process, thousands of charge carriers are excited at the band edges from a single absorbed photon [6].

The radiative recombination of these charge carriers is denoted x-ray excited optical luminescence (XEOL) [15,16]—this is the x-ray analogue to laser-beam-excited photoluminescence (PL). From both XEOL and PL measurements, the optical performance can be evaluated as the local band gap, luminescence yield, and charge-carrier lifetime [17–19]. The emitted photons are usually measured when the solar cell is in the open-circuit state. With a preliminary version of the setup presented in this work, we have demonstrated that fourfold multimodal measurements of a $Cu(In,Ga)Se_2$ solar cell are feasible, including XRF, XBIC, ptychography, and the XEOL intensity [20,21], though without any temporal or spectral sensitivity.

Here, we integrate the upgraded XEOL-detection setup, which we call the "Analyzer of X-ray Excited Optical Luminescence Offering Temporal and spectraL resolution" (AXOLOTL) into the scanning x-ray environment at the microprobe end station of the PETRA III beam line P06. Due to its modular concept, the AXOLOTL setup can be used at various synchrotron end stations or even as stand-alone setup for photoluminescence microscopy.

The XEOL photons are measured in a direct beam path and the signal is resolved spectrally and temporally.

The effectiveness of the AXOLOTL setup is demonstrated with a study on triple-cation mixed-halide perovskite solar cells (PSCs). The stability of perovskites is one of the challenges to be overcome for PSC commercialization [22]. In recent years, mixed-cation perovskites have shown promising results with significantly improved stability compared to early stage metal-halide perovskites [23–27].

While mixing Br on the halide side of $FAPbI_3$ (FA = formamidinium) is most effective in the crystallographic stabilization in favor of α-phase perovskites, density-functional-theory calculations by Kim *et al.* [25] have revealed that the band-gap widening of Br replacing I diminishes the photoconversion efficiency. Therefore, methylammonium (MA) should be introduced on the cation site to reduce the amount of necessary Br. Adding Cs dramatically increases the chemical stability of $FAPbI_3$ [25]. Additionally, the introduction of Cs can lower the trap density and leads to shallower trap states [28,29], suppresses the growth of intermediate phases and promotes the α-phase formation [30,31]. Promising results have been shown by Peng *et al.* [32], who have created PSCs with an absorber composition of $Cs_{0.05}FA_{0.88}MA_{0.07}PbI_{2.56}Br_{0.44}$ and a record efficiency of 23.17%. However, a further increase of the Cs content to around 20% has been reported to result in a decrease in efficiency going hand in hand with halide segregation [29]. Additionally, an increase in Cs can greatly influence the topography of the resulting thin film, leading to the formation of wrinkles [33–36], i.e., thicker and thinner areas in the absorber layer that we denote as *mountains* and *valleys* in the following.

Wrinkle occurrence is generally associated with a relief of compressive strain [34,36]. Wrinkled perovskites have been shown to exhibit inhomogeneous optical performance, with inconsistent results reported in the literature: (i) a band-gap narrowing at mountains [34], with a red shift in the PL peak, or (ii) a band-gap widening at mountains [35], with a blue shift in the PL peak. There are three possible explanations for the inhomogeneous PL response:

(1) *Compositional inhomogeneity.* An increase in Br and Cs content generally widens the band gap [23,37–40]; Bercegol *et al.* have reported on an increased Cs content in the mountains that led to a blue-shifted PL spectrum [35].
(2) *Lattice strain.* Braunger *et al.* [34] have found no compositional variation but systematically larger grains in the mountains. They have associated the observed band-gap narrowing with findings from D'Innocenzo *et al.* [41].
(3) *Reabsorption effects.* As the absorber layer is thicker in the mountains than in the valleys, PL photons have a greater chance to be reabsorbed with subsequent emission of a lower-energy photon, which leads to a red shift of the overall PL spectrum [42–45].

As the composition [35] as well as the preparation method [34] impact on the formation of wrinkles, a large parameter space is given. Hence, each system has to be evaluated individually with the spatially resolved assessment of multiple parameters to establish a causal relationship with the synthesis conditions.

The studies of Braunger *et al.* [34] and Bercegol *et al.* [35] have used different probes for the evaluation of the optical performance (laser), the composition (electrons), and the crystallographic structure (x rays). As electron probes are surface sensitive, while lasers and especially x rays have a deeper penetration depth, their respective beam-sample interaction volumes are not comparable. Therefore, a direct link between local performance and composition or grain structure has not yet been established.

With the AXOLOTL setup included in a multimodal x-ray microscopy measurement scheme, we have exclusively combined x-ray-based techniques to elucidate the local relation between absorber topography, composition, and optical and electrical performance. The advantage of x-ray-based over electron- or ion-based methods is the sensitivity to the full depth of the solar cell with a comparable beam-sample interaction volume for all modalities.

II. RESULTS

A. A novel XEOL spectroscopy setup: AXOLOTL

The addition of optical-luminescence measurements to the suite of raster-scanning techniques offers the possibility of investigating the local optical performance of the device through spectrally (SR) and temporally resolved (TR) XEOL [15,16,46–49]. Measuring XEOL instead of classical PL has its own constraints and considerations. XEOL spectroscopy measurements are challenging due to the small beam-sample interaction volume, low absorption cross section, and considerations of beam damage, which are thoroughly discussed in [8,50].

Existing beam lines such as the hard x-ray nanoprobe 23A at the Taiwan Photon Source [49], the nanoimaging beam line ID16B at the European Synchrotron Radiation Facility [51], or the applied x-ray absorption spectroscopy beam line P65 at PETRA III [52] employ fiber-coupled optics and streak cameras for simultaneous SR- and TR-XEOL measurements. These are not optimized toward detection sensitivity, as is needed for raster scanning beam-damage-sensitive samples such as perovskites with a nanofocused x-ray beam. The AXOLOTL instrument, schematically shown in Fig. 1, has been specifically developed to address this challenge and to offer the highest detection sensitivity. It has been designed to be transportable, compact, and modular for ease of use and adaptation of the instrument to different samples and beam line environments.

Consequently, the whole setup has been built as an optical enclosure upon a breadboard that can be aligned to the sample and other components of the beam line. Further, it can either be controlled as part of the beam-line control system or as an independent detection unit.

The major constraint for multimodal scanning microscopy measurements is the competition for detection solid angle. To efficiently collect the XEOL photons in combination with other detectors, such as XRF or XRD detectors, and for compatibility with transmission-geometry measurements such as ptychography, a large-aperture infinity-corrected objective (1) (see Fig. 1) with a long working distance has been implemented. The lens system has been mounted on a piezo *XYZ* stage for optimal alignment and situated to cover the solid angle upstream of the sample surface as far as the beam-line environment has allowed (10° between the detector and the sample surface; see Fig. S1 of the Supplemental Material [53]). For the detection of the collected photons, the beam has been

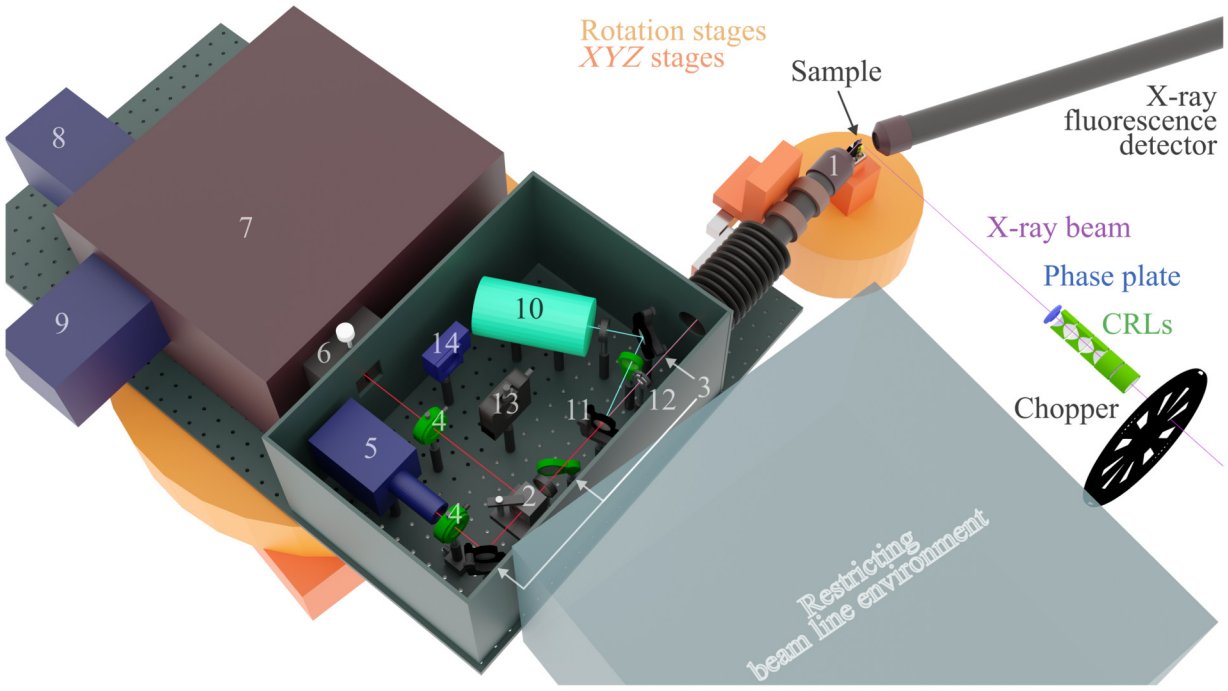

FIG. 1. A schematic representation of the XEOL-detection setup and multimodal measurement approach. Drawn into the scheme are the beam paths: blue for the alignment laser, red for the XEOL photons, and purple for the x-ray beam. For further explanation of the elements, see Sec. IV.

split and directed into two separate detection units, one for TR-XEOL measurements (Fig. 1) (5) and the other for SR-XEOL measurements (7–8).

The TR-XEOL unit consists of an avalanche photodiode (APD) (5) with a time-correlated single-photon-counting (TCSPC) instrument that has been synchronized with the x-ray-beam clock to measure the delay of the XEOL photons relative to the x-ray excitation pulse. A spectrograph (7) in combination with one of two charge-coupled devices (CCDs) (8, 9) has been employed for SR XEOL. Detailed descriptions can be found in Sec. IV.

The alignment of the probe, sample, and detector poses a six-dimensional (6D) problem: the interaction spot of the highly focused x-ray beam [coherent 100 nm (vertical) × 96 nm (horizontal) full width at half maximum (FWHM); see Fig. S2 of the Supplemental Material [53]] with the sample [the first three-dimensional (3D) alignment] and the focus of the AXOLOTL objective with the interaction spot (the second 3D alignment) have to be managed to $<1\,\mu m^3$. Aligning the focus spot of the AXOLOTL setup under a shallow angle increases the difficulty. Thus, an alignment laser and camera have been installed to aid in the 6D positioning of the x-ray-beam–sample–AXOLOTL setup. The laser further offers the possibility of conducting classical PL measurements without the x-ray beam or, potentially, even more sophisticated nanoscale x-ray-pump–laser-probe measurements when synchronized to the bunch clock.

The capability of the AXOLOTL setup will be demonstrated in the following on the multimodal x-ray-based analysis of PSCs.

B. Study of perovskite solar cells

1. Impact of Cs *on the perovskite wrinkling structure*

To study the impact of Cs in PSCs, three cells with varying Cs content have been prepared: the perovskite mixture of the samples is $Cs_xMA_{0.15}FA_{0.85-x}Pb(I_{0.8},Br_{0.2})_3$, with x being 0.05, 0.15, and 0.25. Three representative samples, denoted as *Cs05*, *Cs15*, and *Cs25*, respectively, have been extracted from the cells as fully operational subcells to proceed with x-ray-based measurements. They originate from central positions on the substrates and cells to avoid edge effects and have been selected based on their open-circuit voltage under ambient light.

A decrease in efficiency with increasing Cs content has been observed in laboratory-based measurements of coprocessed sister cells. The J-V curves, with further statistics of the cell-performance parameters, are provided in Figs. S3–S5 of the Supplemental Material [53]. An increase of the band gap and the V_{OC} deficit (Table S1 of the Supplemental Material [53]) for increasing Cs concentration has been derived from external quantum efficiency (EQE) measurements. The decrease in efficiency is assumed to be related to the formation of wrinkles in the absorber. Here, the wrinkles are studied in greater detail, employing x-ray-based multimodal measurements.

For an overview of the samples, the composition and electrical performance have been assessed with XRF and XBIC measurements, respectively. An x-ray beam with an energy of 13.5 keV, slightly above the Br_K edge (13.47 keV) and the Pb_{L3} edge (13.04 keV), has been chosen to ensure a high absorption cross section and a strong XRF signal for Pb (Φ_{Pb}). The Φ_{Pb} signal strength is indicative of the absorber topography—Pb is not competing directly with other elements for its lattice space and a linear relationship between the XRF count rate and the perovskite thickness can be assumed in the thin-film approximation [54,55].

In Fig. 2, we show the distribution of Φ_{Pb} [Figs. 2(a)–2(c)] and the electrical performance as XBIC signal I_{XBIC} [Figs. 2(d)–2(f)]. Additional XBIV measurements are shown in Fig. S6 of the Supplemental Material [53]. The wrinkle structures of Cs15 and Cs25 are visible in the Φ_{Pb} distribution as well as in the I_{XBIC} signal. The maps of I_{XBIC} reveal areas of significantly lower performance [Figs. 2(d)–2(f)] that do not coincide with the wrinkling structure [Figs. 2(a)–2(c)] or with the variations in the XRF signal of any heavy absorber element (Pb, Br, Cs, or I; see Figs. S7–S9 of the Supplemental Material [53]). Areas that are electrically underperforming at the nano- and microscale have been reported earlier. They have been attributed to pinholes in the absorber [56], local trap states acting as recombination centers [57], or other spatial inhomogeneities of interfaces and layers (including charge-selective layers) [58] beyond sensitivity or resolution of the presented XRF measurements. The origin of local underperformance is not at the core of this study; independently of their origin, their prominent and spatially expanded effect on the XBIC measurements is assumed to be due to the large diffusion length of the charge carriers.

The influence of the large diffusion length is further visible in the comparison of the amplitude variations of I_{XBIC} and Φ_{Pb} for Cs15 and Cs25 (see Figs. S10(g) and S10(h) of the Supplemental Material [53]). The periodicity of the wrinkles has been retrieved using fast-Fourier-transformation analysis (see Fig. S10(i) of the Supplemental Material [53]) and a period of $T_f = 18.2\,\mu m$ for Cs15 and of $T_f = 8.3\,\mu m$ for Cs25 has been found. While the period of the XBIC and XRF signal is the same, the difference between the modulation strengths of the two modalities is greater for Cs25 than for Cs15. This can directly be attributed to the smaller wrinkle period and supports the hypothesis of a larger point-spread function of XBIC compared to XRF.

Further, a monotonic increase of the median I_{XBIC} is observed across the series of cells, as evidenced in Fig. S7 of the Supplemental Material [53]. This can likely be attributed to the generally increased charge-collection efficiency related to the overall increased performance that

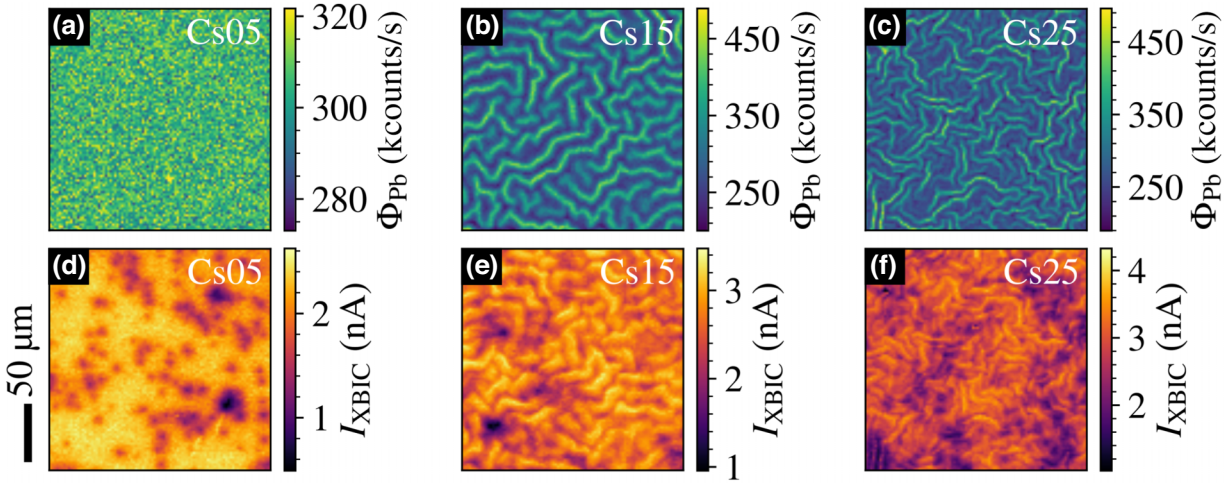

FIG. 2. (a)–(c) The XRF signals of Pb Φ_{Pb} of (a) Cs05, (b) Cs15, and (c) Cs25. (d)–(f) The XBIC signals I_{XBIC} of (d) Cs05, (e) Cs15, and (f) Cs25.

is evidenced by the open-circuit-voltage increase with increasing Cs content (cf. Fig. S4 of the Supplemental Material [53]).

2. Variation of the optical performance over wrinkles

Aside from the formation of wrinkles, PSCs with higher Cs content have shown to undergo a general blue shift of their PL spectra [23,37–39] and to exhibit longer PL lifetimes [35]. This has been linked to a defect-passivating role of Cs [23,28]. While these results indicate a possible improvement of the efficiency for a Cs content around 10%, and Tang *et al.* [29] have found a decrease in efficiency at 20% Cs content, the laboratory measurements of the cells measured here (see Figs. S3–S5 of the Supplemental Material [53]) already indicate a decrease in lifetime for a cell with 15% Cs content.

So far, the role of inhomogeneities within the wrinkled structures has not been clear: Braunger *et al.* [34] have found no significant compositional change from valleys to mountains but Bercegol *et al.* [35] have claimed an increased amount of Cs in mountains; Tang *et al.* [29] have uncovered a segregation of Br- and I-rich phases for PSC with high Cs content, albeit without spatial resolution. Thus, whether or not the two phases are associated with the wrinkle topography has been left to speculation.

To elucidate these aspects, the XRF signal for the spatial assessment of the composition as well as XEOL for the recombination yield, band gap, and lifetime of the charge carriers have been measured with high spatial resolution. An area of 20 µm × 20 µm has been raster scanned (for further details, see Sec. IV D).

In the following, we discuss the findings using Cs15 as an example and refer to the Supplemental Material for additional XRF maps and the measurements of Cs05 and Cs25 (see Figs. S11–S14 of the Supplemental Material [53]).

In Fig. 3(a), we show the distribution of the XRF Pb count rate Φ_{Pb}, which reflects the thickness of the absorber. A horseshoelike wrinkle structure is visible. The ratio of the XRF Br count rate Φ_{Br} to Φ_{Pb} is shown in Fig. 3(b) and exhibits the same horseshoelike feature. If the absorber matrix was homogeneous over the scanned area, the Φ_{Br}/Φ_{Pb} ratio should not contain any spatial features; in particular, since the energy of both the Pb_{L3} and Br_K absorption edges is high enough such that self-absorption effects are not strong enough to explain the Φ_{Br}/Φ_{Pb} variations (see Sec. IV E.). Therefore, we conclude that the valleys are Br rich, while the mountains have an accordingly higher I content. The demixing of Br and I itself is a known phenomenon for perovskites [29,59,60].

In Fig. 3(c), we show the central wavelength λ_{cen} of the Gaussian-fitted XEOL spectrum (for corresponding maps of all fit parameters, see Fig. S15 of the Supplemental Material [53]). The scanned area shows a variation of around 10 nm in λ_{cen}, indicating a band-gap narrowing of approximately 20 meV from valley to mountain. This is similar to the results of Braunger *et al.* [34]; here, however, the red shift can be directly linked to the segregation of Br and I as observed in Fig. 3(b). A contour of $\lambda_{cen} = 734$ nm has been overlaid from Fig. 3(c) onto Figs. 3(a) and 3(b) to highlight the correlation. The contour clearly relates the red-shifted area to the thicker absorber [Fig. 3(a)] and the Br-poor area [Fig. 3(b)]. This has led to the conclusion that the red shift at mountains compared to valleys is mainly caused by the compositional segregation into Br-poor and Br-rich regions.

Photon recycling via self-absorption has been considered as an alternative cause for the red shift of λ_{cen}. By taking the detector geometry into account and comparing

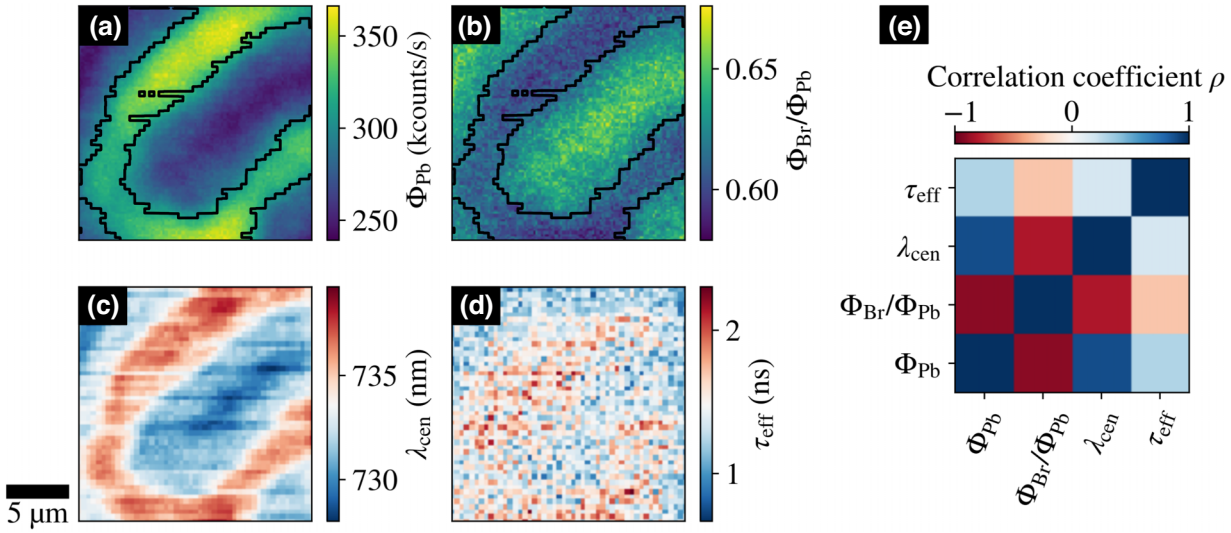

FIG. 3. The XRF and XEOL analysis of cell Cs15. (a) The XRF Φ_{Pb} signal. (b) The XRF Φ_{Br}/Φ_{Pb} ratio. (c) The central wavelength λ_{cen} from SR-XEOL measurements. (d) The effective lifetime τ_{eff} from TR-XEOL measurements upon fitting the decay with two exponentials. (e) Pearson's correlation coefficient ρ.

the amplitude of the XEOL signal as well as the topography (and thus the orientation of the emitting solid angle), we conclude that this is a negligible effect in our case (for the full discussion of this topic, see Sec. S7B and Fig. S17 of the Supplemental Material [53]).

The TR-XEOL decay curves, measured simultaneously with the SR XEOL, have been fitted with a double-exponential function. Maps showing the individual fitting parameters are given in Fig. S17 of the Supplemental Material [53]. In Fig. 3(d), we show the effective lifetime τ_{eff} calculated from the amplitudes and time constants of the fit (see Sec. IV G) for Cs15. A slight trend to longer effective lifetimes in areas with a thicker absorber is observed.

We present two hypotheses pertaining to the increase in the lifetime in the mountains:

(1) The mountains could have fewer bulk and surface defects than the valleys, which would prolong the effective lifetime. This reduction of defects is linked to an increase in Cs as suggested by Bercegol *et al.* and in accordance with previous findings [34–36], as Cs has a passivating effect [28].

(2) The AXOLOTL setup features high-numerical-aperture optics and the TR-XEOL measurement is done in a confocal approach. Hence, recombination is only measured from those charge carriers that recombine spatially within the focus spot; carriers that diffuse or drift out of the focus spot will not be detected. Consequently, the measured amount of radiative recombination as well as the lifetime appear too low for materials with a large diffusion length and lifetime. As the band gap is narrower in the mountains, there is a lower probability that charge carriers will drift out of mountains into the wide-band-gap valleys than vice versa, which leads to a longer effective lifetime. This is in accordance with the findings observed by Frohna *et al.* [59].

In Fig. 3(e), we show the statistical correlations between Figs. 3(a)–3(d) as Pearson's correlation coefficient ρ. Here, 1 indicates perfect positive correlation, 0 no correlation, and −1 perfect anticorrelation. The strong anticorrelation between Φ_{Pb} and the Φ_{Br}/Φ_{Pb} ratio highlights that the local thickness variation of the absorber is associated with the separation into Br-rich and Br-poor regions. Accordingly, the strong anticorrelation between the central wavelength λ_{cen} and the Φ_{Br}/Φ_{Pb} ratio corroborates the segregation hypothesis. The correlation coefficients of τ_{eff} are weaker than the others, which is partly rooted in the higher noise of Fig. 3(d) compared to the other maps. Nevertheless, the trend to longer effective charge-carrier lifetimes at thicker absorber areas is evident in the positive correlation between Φ_{Pb} and τ_{eff}.

3. Overall impact of Cs *on the optical performance*

The spatially resolved evaluation of the three PSCs has not only revealed an intracell inhomogeneity in the optical performance but also an intercell shift toward a broader distribution of the effective lifetime as well as the band gap with higher Cs content. In Fig. 4(a), the histograms of the effective lifetime are depicted as violin plots (τ_{eff} on the vertical axis). The effective lifetime increases from Cs05 to Cs15, while Cs25 has a slightly lower median effective lifetime than Cs15 but also a broader distribution.

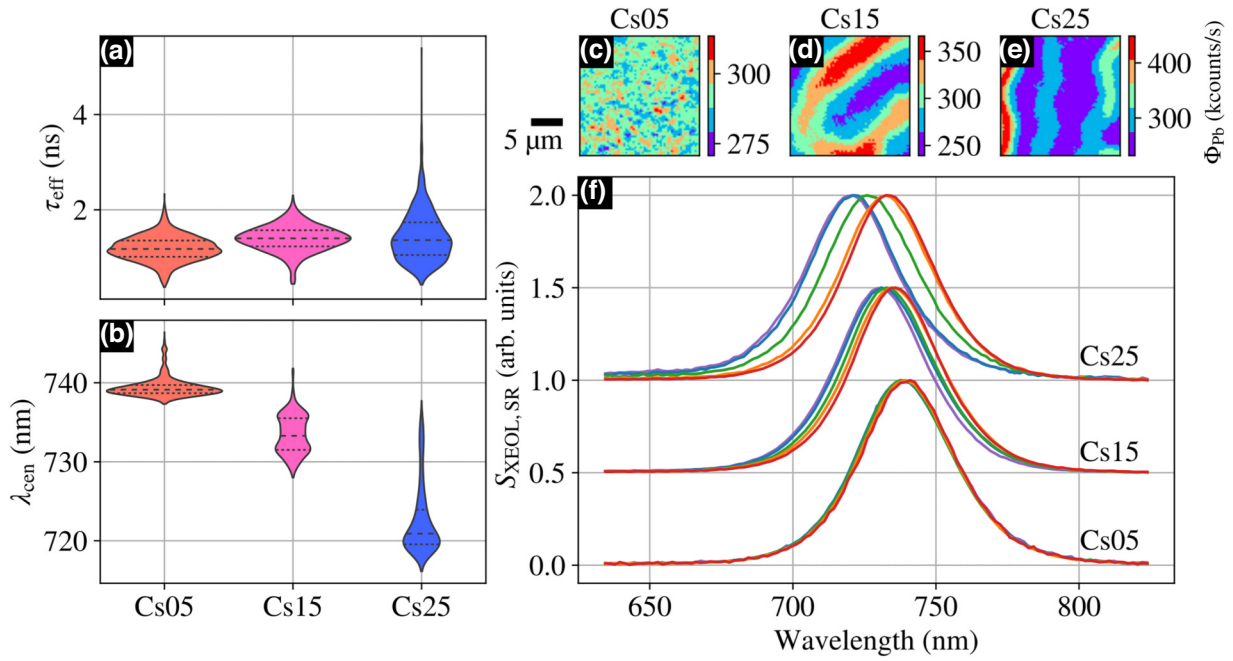

FIG. 4. A comparison of the optical performance of the three PSCs, Cs05, Cs15, and Cs25. (a) The distribution of the effective lifetimes as violin plots; the dashed lines indicate the 25th, 50th, and 75th percentiles. (b) The distribution of the central wavelength as violin plots; the dashed lines indicate the 25th, 50th, and 75th percentiles. (c) The Φ_{Pb} count rate of Cs05. (d) The Φ_{Pb} count rate of Cs15. (e) The Φ_{Pb} count rate of Cs25. (f) Area-averaged XEOL spectra corresponding to the colored areas in (c)–(e), respectively.

Figure 4(b) similarly displays violin plots of the central-wavelength (λ_{cen}) distribution of the XEOL spectra. The blue-shifting effect of Cs as well as an increasing spread in the distribution is evident when comparing the three violins. The average peak position of the Gaussian fit is 739 nm for Cs05, 733 nm for Cs15, and 722 nm for Cs25, showing the same trend of roughly 10 nm in blue shift per 10% of Cs, as noted in the literature [23,37–39]. The red-side end of the distribution shifts less than 10 nm, while the bulk of the distribution shifts almost 20 nm. Overall, the energy corresponding to the mean value of λ_{cen} is slightly higher than the laboratory-based E_g values (see Table S1 of the Supplemental Material [53]) from EQE measurements. This could be due to a higher local filling of the electronic states in the conduction band by the particle shower compared to laser-based excitation. This would lead to recombination from states higher than the conduction-band minimum, explaining the discrepancies between the PL- and XEOL-based estimations of the band gap.

The influence of beam damage to the XEOL spectra has been considered in the choice of beam intensity (see Sec. IV B) and a comparison of full beam intensity and low beam intensity is shown in Fig. S18 of the Supplemental Material [53]. High beam intensity leads to a strong blue shift and deviation of the XEOL spectra from a Gaussian shape. A shoulder at higher energies appears, which is partly attributed to the higher local filling of the electronic states in the conduction band. The observation of this shift to higher energies with a strong beam intensity corroborates the hypothesis that even at a low x-ray-beam flux, the local filling is greater than during the EQE measurements, thus leading to a seemingly wider band gap.

The spectral shift in correlation with the absorber thickness is highlighted in Figs. 4(c)–4(f). The maps in Figs. 4(c)–4(e) show the Pb XRF signal Φ_{Pb} with a discrete color scale to indicate binned areas for which the averaged XEOL spectra are plotted in Fig. 4(f). Here, it appears that the red-side edge is hardly shifted at all, while the blue side is shifting more strongly for higher-Cs-containing PSCs. This nonintuitive "pinning" of the red side could be explained by the iodine increase in the mountain areas, countering the blue shift induced by higher Cs content. In the valley areas, the cumulative effect of the increased Br content and the overall increase in Cs further promote the strong blue shift of the XEOL spectra.

In addition to the statistical correlations between elemental distributions and local performance, in the cell Cs25 we have observed submicrometer small spots with a surplus of Cs and a deficit of Br. These spots are assumed to originate from the CsI precursor and feature a red shift of the XEOL signal compared to the surrounding area, which is expected from the Br deficiency (for further details, see Sec. VI B of the Supplemental Material [53]).

III. DISCUSSION

The novel AXOLOTL detection unit for combined SR and TR XEOL has been used in a multimodal hard x-ray scanning microscopy setup to study the wrinkled structure of PSCs containing varying amounts of Cs (Cs15 and Cs25). Initial laboratory-based measurements have indicated that the overall efficiency of a PSC decreases with increasing Cs content, which we speculate to be caused by the wrinkling of the absorber. The spatially resolved optical performance of the cells has been measured with the AXOLOTL instrument to elucidate the cause of the inhomogeneous PL previously reported for these systems [34,35].

The multimodal approach has allowed us to relate the segregation of I and Br to thick and thin absorber areas, respectively, which we have identified as the primary cause of the band narrowing in the mountain and the band widening in the valley areas.

With these findings, we have demonstrated that the AXOLOTL setup is able to evaluate beam-sensitive materials such as perovskites. By performing multimodal simultaneous XEOL and XRF measurements, the optical performance has been directly linked with the composition, eliminating the drawbacks of separate measurements—a major advantage of XEOL over classical PL.

After demonstrating the multimodal compatibility of our setup in this study, we can envision further experiments encompassing more modalities. A first logical extension would be the inclusion of x-ray diffraction to verify the impact of inhomogeneous lattice spacing on the optical performance. A challenge for the measurements will be that the random orientation of the grains in the absorber only allows the evaluation of those few grains that coincidentally fulfill the Bragg condition.

With the introduction of fourth-generation synchrotrons, ptychography appears as a feasible addition to our multimodal suite, as the demand for a coherent beam would no longer limit the photon flux.

Going a step further, employing heating stages as demonstrated by Chakraborty *et al.* [61] would be an option for investigating solar cells *in situ*. With the alignment laser already present in the AXOLOTL instrument, simultaneous use of the laser and x-ray beam could further be an option, with the two beams acting as either pump or probe. Overall, multimodal hard x-ray scanning microscopy measurement schemes offer an opportunity to directly probe the spatially resolved correlations between composition, structure, and performance to provide insights into semiconductor devices. In view of such correlations elucidating the materials paradigm, the modular AXOLOTL setup is designed to be used at various synchrotron beam lines, adding to the capacity for temporal and spectral optical-luminescence measurements.

IV. EXPERIMENTAL PROCEDURES

A. Sample preparation

For the PSC fabrication, indium tin oxide- (ITO) covered glass (sheet resistance: 15 Ω/sq, XinYan Technologies) substrates have been sonicated in water-acetone-IPA (isopropyl alcohol) baths, prior to a 10-min UV-ozone treatment to clean the surface. The NiO_x hole-transport layer (HTL) (20 nm) has been deposited via rf magnetron sputtering, following a well-established procedure [62]. The perovskite layer (approximately 500 nm) has been deposited under a nitrogen atmosphere via spin coating of perovskite solutions of $Cs_xMA_{0.15}FA_{0.85-x}Pb(I_{0.8},Br_{0.2})_3$ (1 M) in a cosolvent of dimethyl formamide (DMF)–dimethyl sulfoxide (DMSO) (4:1 v/v). Here, a two-step spin-coating process with 2000 rpm for 10 s and 5000 rpm for 30 s has been used. During the second step, after 10 s, 300 µl of chlorobenzene has been dropped as an antisolvent. The films have been subsequently annealed at 100 °C for 25 min. The C_{60} electron-transport layer (ETL) (20 nm, nano-C), 5 nm of bathocuproine (BCP, Sigma-Aldrich), and 100-nm silver contacts have been deposited via thermal evaporation (Angstrom Engineering) within the same deposition chamber, as reported previously [63].

B. Experimental settings

The x-ray measurements have been conducted at the hard x-ray micro-/nanoprobe beam line P06 (microprobe end station) at Petra III (DESY, Germany) using a beam energy of 13.5 keV. As sketched in Fig. 1, the x-ray beam has passed a retractable optical chopper (MC2000B with MC1F10HP, Thorlabs), running at 813 Hz, to enable the use of a lock-in amplifier (UHFLI, Zurich Instruments) for the XBIC measurements. After the chopper, the beam has been guided through the focusing optics, which have consisted of 50 Be-CRLs (compound refractive lenses) [64], a phase plate, and a 400-µm pinhole. The coherent part of the beam had a spot size of 100 nm (vertical) × 96 nm (horizontal) FWHM. The sample surface has been oriented perpendicular to the beam path to minimize the beam footprint. A fluorescence detector (Vortex-ME4, Hitachi) has been situated opposite the XEOL detector with a central angle of 47.6° to the sample surface. The sample has been mounted and electrically contacted on a printed circuit board and fastened to a kinematic mount (KB25/M, Thorlabs) as described in Ref. [11]. The XEOL-detection unit has been angled to the sample at 10°.

C. AXOLOTL

The setup is described following the numbering in Fig. 1. For the coarse alignment with respect to the x-ray beam and the beam line itself, the breadboard that hosts the optical setup has been installed on top of

a manual rotation stage and motorized *XYZ* translation stages. An infinity-corrected long-working-distance objective (Olympus LMPLFLN100X, NA = 0.8) (1), connected to a lens tube, has been mounted to piezo-motors (PI) for the fine alignment. The XEOL signal collected from the sample has been divided into two parts by a 50:50 beam splitter (KM200B/M, Thorlabs) (2). One part has been focused (lens AC254-100-A, mounted in translation lens mount LM1XY, Thorlabs) (4) onto an APD (PDM Series, Mirco Photon Devices) (5); the other part has been focused on the entrance slit of a spectrograph (6).

The signal from the APD has been fed into a TCSPC module (PicoHarp 300, PicoQuant) for TR-XEOL measurements and to the counter of the beam-line system for fast intensity evaluation.

The spectrograph (Acton SpectraPro Series, model 2300i, Princeton Instruments) (7) with either a mirror or a 300 gr/mm grating (750-nm blaze) selected, has guided the light onto one of two of the CCD cameras: (iDus420OE, Andor) (8) or (ProEM 512, Princeton Instruments) (9). The two cameras have been installed to account for either fast imaging of the spot emitting the XEOL signal for the proper alignment (ProEM512) or for low-noise experiments (iDus420OE). Both cameras contain a Si chip suitable for the visible–near-infrared spectral range. As the whole system is modular, individual components (cameras, mirrors, gratings, filters, etc.) are easily interchangeable to cover other wavelength regions of interest.

A simple imaging camera (webcam with dismounted lens) (14) and a laser (440 nm, LDH-P-C-440, Picoquant with laser driver PDL 800-D) (10) have been incorporated into the system for initial coarse alignment of the system to the x-ray-beam–sample interaction spot. The laser beam has been attenuated by a neutral density filter and filtered by a 450-nm short-pass filter (FES450, Thorlabs). Mirrors (3) have guided the beam to a beam splitter (10:90) (11) and the smaller fraction further through an iris (ID12, Thorlabs) (12) to the entrance aperture of the objective.

Using a flip mirror (3), the light collected from the sample could be either focused on the webcam (14) by a lens to inspect the focus of the alignment laser or on the aforementioned CCD (8, 9) and APD (5) detectors.

For conventional PL measurements, a 450-nm long-pass filter (FELH 450, Thorlabs) has been placed in front of the 50:50 beam splitter (2) to suppress the laser light.

Both the APD and CCD cameras have been controlled and read out by a personal computer that was independent of the beam-line controls. Synchronization has been obtained by trigger signals from the electron bunch clock and from scan positions. Contingent on the time profile of the x-ray pulses, an effective time resolution of 64 ps has been experimentally achieved with a nominal x-ray pulse duration of 44 ps and a nominal timing resolution of the APD of 50 ps. The spectral resolution of the SR-XEOL setup was 1.7 nm and the spatial resolution around 500 nm (close to diffraction limited).

D. Measurement settings

The XRF measurements have been conducted at full beam intensity. For the dedicated XBIC and XEOL measurements, the beam intensity has been attenuated to only 1% to limit the x-ray-induced degradation and excitation levels, both of which are discussed in Sec. VIII of the Supplemental Material [53] and in the literature [8,50,65–67].

All maps in Fig. 2 have been measured in 1-μm steps, with a dwell time of 25 ms. The XEOL maps in Fig. 3 have been measured in 400-nm steps with a dwell time of 1.0 s. The XRF maps in Fig. 3 have been measured in 200-nm steps with a dwell time of 0.3 s.

E. XRF analysis

The energy of the incident photons has been chosen in a trade-off between the availability of x-ray optics with a long working distance and a small spot size, x-ray flux, self-absorption, and sensitivity to all critical elements (Pb, Br, I, and Cs). This is not ideal for the quantification of iodine and cesium, where the evaluation needs to rely on the XRF signal from the *L* edges and the quantification is heavily impaired by self-absorption. Hence, the signal detection for Cs and I is to be seen critically, as both have a low absorption cross section at the excitation energy and suffer from self-absorption effects. Therefore, our conclusions uniquely rely on the Br-Pb distribution. The Br and Pb distributions have been obtained from similar energies in the XRF spectra (Br_K, 11.9–13.5 keV; Pb_L, 9.2–15.2 keV). At these energies, self-absorption has had a similar effect on the Br and Pb quantification and is negligible.

The fitting of the XRF spectra has been done with PyMca [68]. The four detection channels of the Vortex-ME4 have been fitted individually and summed after fitting. Based on a layered model of the cells, we have applied a self-absorption correction during the fitting process in PyMca following a similar approach as in Ref. [69]. However, this is of limited value, as it cannot adequately reflect the spatial variations in absorber thickness due to the wrinkling structure.

F. XEOL spectra fitting

The XEOL spectra have been fitted with a Gaussian function of the form

$$G(x) = A \cdot \exp\left\{-\frac{1}{2}\frac{(x-x_0)^2}{\sigma^2}\right\} + C, \tag{1}$$

where A is the amplitude, x_0 is the central wavelength, σ is the standard deviation, and C is an offset accounting for the dark counts in the spectrograph.

G. XEOL decay fitting

We have used a conventional approach [70] for fitting luminescence decay curves with two exponential functions but additionally convoluted them with the Gaussian response function of the detector.

For a single exponential decay convoluted with a Gaussian function, the analytical solution is given as

$$S(t) = \frac{A}{2}\exp\left(-\frac{t}{\tau}\right)\exp\left(\frac{\sigma^2}{2\tau^2}\right) \cdot \operatorname{erfc}\left(\frac{\sigma}{\sqrt{2}\tau} - \frac{t}{\sigma\sqrt{2}}\right) + C, \tag{2}$$

where A is the amplitude, τ is the decay constant, σ is the parametrization of the Gaussian width, and C is an offset to consider dark counts. The complementary error function $\operatorname{erfc}(x) = 1 - \operatorname{erf}(x)$ is derived from the error function

$$\operatorname{erf}(x) = \frac{2}{\sqrt{\pi}}\int_0^x \exp\left(-t^2\right) \mathrm{d}t. \tag{3}$$

The extension to a model with two exponentials is trivial, as it is a simple summation, leading to the fitting function

$$S(t) = \frac{A_1}{2}\exp\left(-\frac{t}{\tau_1}\right)\exp\left(\frac{\sigma^2}{2\tau_1^2}\right)\operatorname{erfc}\left(\frac{\sigma}{\sqrt{2}\tau_1} - \frac{t}{\sigma\sqrt{2}}\right) + \frac{A_2}{2}\exp\left(-\frac{t}{\tau_2}\right)\exp\left(\frac{\sigma^2}{2\tau_2^2}\right) \times \operatorname{erfc}\left(\frac{\sigma}{\sqrt{2}\tau_2} - \frac{t}{\sigma\sqrt{2}}\right) + C. \tag{4}$$

The effective lifetime has been calculated from the amplitudes and their respective decay time constants as

$$\tau_{\text{eff}} = \frac{\sum_i A_i\tau_i^2}{\sum_i A_i\tau_i}. \tag{5}$$

By using a multiple-step procedure, we have aligned our decay curves to the same excitation time. This was necessary as the start point oscillates between two bins of our TCSPC unit (see Fig. S17 of the Supplemental Material [53]).

The data sets generated during and/or analyzed during the current study are available from the corresponding author on reasonable request.

ACKNOWLEDGMENTS

We acknowledge DESY (Hamburg, Germany), a member of the Helmholtz Association HGF, for the provision of experimental facilities. Parts of this research were carried out at beam line P06. This research was supported in part through the Maxwell computational resources operated at DESY. Beam time was allocated for the proposal ID I-20170000.

We gratefully acknowledge Stephan Botta, Ralph Döhrmann, Patrik Wiljes, Niklas Pyrlik, and Giovanni Fevola (DESY, Germany) for technical support and fruitful discussions, as well as Jan Siebels (Universität Hamburg) for support during the measurements.

C.O., C.S., J.F., A.M., C.G.S., T.K., and M.E.S. designed the study and the instrument. C.O., C.S., J.F., S.P., J.G., K.M.S., J.H., F.S., G.F., T.K., and M.E.S. conducted the measurements. M.D.B., E.A., F.H.I., and S.D.W. prepared the samples. C.O., C.S., T.K., and M.E.S. prepared the manuscript. All authors were involved with feedback and discussions about the manuscript and data analysis.

The authors declare no competing interests.

[1] C. Lamberti, The use of synchrotron radiation techniques in the characterization of strained semiconductor heterostructures and thin films, Surf. Sci. Rep. **53**, 1 (2004).

[2] G. Martínez-Criado, J. Segura-Ruiz, B. Alén, J. Eymery, A. Rogalev, R. Tucoulou, and A. Homs, Exploring single semiconductor nanowires with a multimodal hard x-ray nanoprobe, Adv. Mater. **26**, 7873 (2014).

[3] L. Chayanun, S. Hammarberg, H. Dierks, G. Otnes, A. Björling, M. T. Borgström, and J. Wallentin, Combining nanofocused x-rays with electrical measurements at the NanoMAX beamline, Crystals **9**, 1 (2019).

[4] C. E. Murray, H. Yan, C. Lavoie, J. Jordan-Sweet, A. Pattammattel, K. Reuter, M. Hasanuzzaman, N. Lanzillo, R. Robison, and N. Loubet, Mapping of the mechanical response in Si/SiGe nanosheet device geometries, Nat. Commun. Eng. **1**, 1 (2022).

[5] T. Buonassisi, A. A. Istratov, M. A. Marcus, B. Lai, Z. Cai, S. M. Heald, and E. R. Weber, Engineering metal-impurity nanodefects for low-cost solar cells, Nat. Mater. **4**, 676 (2005).

[6] M. E. Stuckelberger, B. West, T. Nietzold, B. Lai, J. M. Maser, V. Rose, and M. I. Bertoni, Review: Engineering solar cells based on correlative x-ray microscopy, J. Mater. Res. **32**, 1825 (2017).

[7] J.-P. Correa-Baena, Y. Luo, T. M. Brenner, J. Snaider, S. Sun, X. Li, M. A. Jensen, N. T. P. Hartono, L. Nienhaus, S. Wieghold, *et al.*, Homogenized halides and alkali cation segregation in alloyed organic-inorganic perovskites, Science **363**, 627 (2019).

[8] M. Kodur, R. E. Kumar, Y. Luo, D. N. Cakan, X. Li, M. E. Stuckelberger, and D. P. Fenning, X-ray microscopy of halide perovskites: Techniques, applications, and prospects, Adv. Energy. Mater. **10**, 1903170 (2020).

[9] H. Hieslmair, A. A. Istratov, R. Sachdeva, and E. R. Weber, in *10th Workshop on Crystalline Silicon Solar Cell Materials and Processes* (National Renewable Energy

Laboratory (NREL), Copper Mountain, Colorado, 2000), p. 162, https://www.nrel.gov/docs/fy00osti/28844.pdf.

[10] M. Stuckelberger, T. Nietzold, B. M. West, B. Lai, J. Maser, V. Rose, and M. I. Bertoni, in *Proc. Photovoltaic Specialist Conference (PVSC)* (IEEE, Washington, DC, 2017), p. 2179.

[11] C. Ossig, T. Nietzold, B. M. West, M. I. Bertoni, G. Falkenberg, C. G. Schroer, and M. E. Stuckelberger, X-ray beam induced current measurements for multi-modal x-ray microscopy of solar cells, J. Vis. Exp. **150**, e60001 (2019).

[12] G. E. Eperon, D. Moerman, and D. S. Ginger, Anticorrelation between local photoluminescence and photocurrent suggests variability in contact to active layer in perovskite solar cells, ACS Nano **10**, 10258 (2016).

[13] R. Hosseinian Ahangharnejhad, Z. Song, T. Mariam, J. J. Gardner, G. K. Liyanage, Z. S. Almutawah, B. M. M. Anwar, M. Junda, N. J. Podraza, A. B. Phillips, *et al.*, Protecting perovskite solar cells against moisture-induced degradation with sputtered inorganic barrier layers, ACS Appl. Energy Mater. **4**, 7571 (2021).

[14] J. Cazaux, A physical approach to the radiation damage mechanisms induced by x-rays in x-ray microscopy related techniques, J. Microsc. **188**, 106 (1997).

[15] S. Emura, T. Moriga, J. Takizawa, M. Nomura, K. R. Bauchspiess, T. Murata, K. Harada, and H. Maeda, Optical-luminescence yield spectra produced by x-ray excitation, Phys. Rev. B **47**, 6918 (1993).

[16] T.-K. Sham and R. A. Rosenberg, Time-resolved synchrotron radiation excited optical luminescence: Light-emission properties of silicon-based nanostructures, ChemPhysChem **8**, 2557 (2007).

[17] S. Siebentritt, T. P. Weiss, M. Sood, M. H. Wolter, A. Lomuscio, and O. Ramirez, How photoluminescence can predict the efficiency of solar cells, J. Phys. Mater. **4**, 040210 (2021).

[18] T. Kirchartz, J. A. Márquez, M. Stolterfoht, and T. Unold, Photoluminescence-based characterization of halide perovskites for photovoltaics, Adv. Energy Mater. **10**, 1904134 (2020).

[19] A. R. Bowman and S. D. Stranks, How to characterize emerging luminescent semiconductors with unknown photophysical properties, PRX Energy **2**, 022001 (2023).

[20] C. Ossig, C. Strelow, J. Flügge, A. Kolditz, J. Siebels, J. Garrevoet, K. Spiers, M. Seyrich, D. Brückner, N. Pyrlik, *et al.*, Four-fold multi-modal x-ray microscopy measurements of a Cu(In,Ga)Se_2 solar cell, Materials **14**, 228 (2021).

[21] G. Fevola, C. Ossig, M. Verezhak, J. Garrevoet, H. L. Guthrey, M. Seyrich, D. Brückner, J. Hagemann, F. Seiboth, A. Schropp, *et al.*, 3D and multimodal x-ray microscopy reveals the impact of voids in CIGS solar cells, Adv. Sci. **11**, 2301873 (2024).

[22] Y. Rong, Y. Hu, A. Mei, H. Tan, M. I. Saidaminov, S. I. Seok, M. D. McGehee, E. H. Sargent, and H. Han, Challenges for commercializing perovskite solar cells, Science **361**, eaat8235 (2018).

[23] M. Saliba, T. Matsui, J.-Y. Seo, K. Domanski, J.-P. Correa-Baena, M. K. Nazeruddin, S. M. Zakeeruddin, W. Tress, A. Abate, A. Hagfeldt, *et al.*, Cesium-containing triple cation perovskite solar cells: Improved stability, reproducibility and high efficiency, Energy Environ. Sci. **9**, 1989 (2016).

[24] M. Salado, M. A. Fernández, J. P. Holgado, S. Kazim, M. K. Nazeeruddin, P. J. Dyson, and S. Ahmad, Towards extending solar cell lifetimes: Addition of a fluorous cation to triple cation-based perovskite films, ChemSusChem **10**, 3846 (2017).

[25] S. Kim, T. Eom, Y.-S. Ha, K.-H. Hong, and H. Kim, Thermodynamics of multicomponent perovskites: A guide to highly efficient and stable solar cell materials, Chem. Mater. **32**, 4265 (2020).

[26] M. M. Byranvand, C. Otero-Martínez, J. Ye, W. Zuo, L. Manna, M. Saliba, R. L. Z. Hoye, and L. Polavarapu, Recent progress in mixed A-site cation halide perovskite thin-films and nanocrystals for solar cells and light-emitting diodes, Adv. Opt. Mater. **10**, 2200423 (2022).

[27] E. Aydin, T. G. Allen, M. De Bastiani, A. Razzaq, L. Xu, E. Ugur, J. Liu, and S. De Wolf, Pathways toward commercial perovskite/silicon tandem photovoltaics, Science **383**, eadh3849 (2024).

[28] Y. Hu, E. M. Hutter, P. Rieder, I. Grill, J. Hanisch, M. F. Aygüler, A. G. Hufnagel, M. Handloser, T. Bein, A. Hartschuh, *et al.*, Understanding the role of cesium and rubidium additives in perovskite solar cells: Trap states, charge transport, and recombination, Adv. Energy Mater. **8**, 1703057 (2018).

[29] M.-C. Tang, Y. Fan, D. Barrit, R. Li, H. X. Dang, S. Zhang, T. J. Magnanelli, N. V. Nguyen, E. J. Heilweil, C. A. Hacker, *et al.*, Efficient hybrid mixed-ion perovskite photovoltaics: In situ diagnostics of the roles of cesium and potassium alkali cation addition, Solar RRL **4**, 2000272 (2020).

[30] S. De Wolf, J. Holovsky, S.-J. Moon, P. Löper, B. Niesen, M. Ledinsky, F.-J. Haug, J.-H. Yum, and C. Ballif, Organometallic halide perovskites: Sharp optical absorption edge and its relation to photovoltaic performance, J. Phys. Chem. Lett. **5**, 1035 (2014).

[31] H. X. Dang, K. Wang, M. Ghasemi, M.-C. Tang, M. De Bastiani, E. Aydin, E. Dauzon, D. Barrit, J. Peng, D.-M. Smilgies, *et al.*, Multi-cation synergy suppresses phase segregation in mixed-halide perovskites, Joule **3**, 1746 (2019).

[32] J. Peng, D. Walter, Y. Ren, M. Tebyetekerwa, Y. Wu, T. Duong, Q. Lin, J. Li, T. Lu, M. A. Mahmud, *et al.*, Nanoscale localized contacts for high fill factors in polymer-passivated perovskite solar cells, Science **371**, 390 (2021).

[33] K. Sveinbjörnsson, K. Aitola, J. Zhang, M. B. Johansson, X. Zhang, J.-P. Correa-Baena, A. Hagfeldt, G. Boschloo, and E. M. J. Johansson, Ambient air-processed mixed-ion perovskites for high-efficiency solar cells, J. Mater. Chem. A **4**, 16536 (2016).

[34] S. Braunger, L. E. Mundt, C. M. Wolff, M. Mews, C. Rehermann, M. Jost, A. Tejada, D. Eisenhauer, C. Becker, J. Andres Guerra, *et al.*, $Cs_xFA_{1-x}Pb(I_{1-y}Br_y)_3$ perovskite compositions: The appearance of wrinkled morphology and its impact on solar cell performance, J. Phys. Chem. C **122**, 17123 (2018).

[35] A. Bercegol, F. J. Ramos, A. Rebai, T. Guillemot, J.-B. Puel, J.-F. Guillemoles, D. Ory, J. Rousset, and L. Lombez,

Spatial inhomogeneity analysis of cesium-rich wrinkles in triple-cation perovskite, J. Phys. Chem. C **122**, 23345 (2018).

[36] S.-G. Kim, J.-H. Kim, P. Ramming, Y. Zhong, K. Schötz, S. J. Kwon, S. Huettner, F. Panzer, and N.-G. Park, How antisolvent miscibility affects perovskite film wrinkling and photovoltaic properties, Nat. Commun. **12**, 1554 (2021).

[37] X. Yu, T. Liu, Q. Wei, C. Liang, K. Wang, J. Guo, D. Zhao, B. Wang, R. Chen, and G. Xing, Tailoring the surface morphology and phase distribution for efficient perovskite electroluminescence, J. Phys. Chem. Lett. **11**, 5877 (2020).

[38] S. Ašmontas, A. Čerškus, J. Gradauskas, A. Grigucevičienė, K. Leinartas, A. Lučun, K. Petrauskas, A. Selskis, A. Sužiedėlis, E. Širmulis, *et al.*, Cesium-containing triple cation perovskite solar cells, Coatings **11**, 279 (2021).

[39] C. Wang, Z. Song, Y. Yu, D. Zhao, R. A. Awni, C. R. Grice, N. Shrestha, R. J. Ellingson, X. Zhao, and Y. Yan, Synergistic effects of thiocyanate additive and cesium cations on improving the performance and initial illumination stability of efficient perovskite solar cells, Sustain. Energy Fuels **2**, 2435 (2018).

[40] R. J. Sutton, G. E. Eperon, L. Miranda, E. S. Parrott, B. A. Kamino, J. B. Patel, M. T. Hörantner, M. B. Johnston, A. A. Haghighirad, D. T. Moore, *et al.*, Bandgap-tunable cesium lead halide perovskites with high thermal stability for efficient solar cells, Adv. Energy Mater. **6**, 1502458 (2016).

[41] V. D'Innocenzo, A. R. S. Kandada, M. De Bastiani, M. Gandini, and A. Petrozza, Tuning the light emission properties by band gap engineering in hybrid lead halide perovskite, J. Am. Chem. Soc. **136**, 17730 (2014).

[42] J. M. Richter, M. Abdi-Jalebi, A. Sadhanala, M. Tabchnyk, J. P. Rivett, L. M. Pazos-Outón, K. C. Gödel, M. Price, F. Deschler, and R. H. Friend, Enhancing photoluminescece yields in lead halide perovskites by photon recycling and light out-coupling, Nat. Commun. **7**, 13941 (2016).

[43] F. Staub, U. Rau, and T. Kirchartz, Statistics of the Auger recombination of electrons and holes via defect levels in the band gap—application to lead-halide perovskites, ACS Omega **3**, 8009 (2018).

[44] M. Wang, K. Wang, Y. Gao, J. I. Khan, W. Yang, S. De Wolf, and F. Laquai, Impact of photoluminescence reabsorption in metal-halide perovskite solar cells, Solar RRL **5**, 2100029 (2021).

[45] P. Fassl, V. Lami, F. J. Berger, L. M. Falk, J. Zaumseil, B. S. Richards, I. A. Howard, Y. Vaynzof, and U. W. Paetzold, Revealing the internal luminescence quantum efficiency of perovskite films via accurate quantification of photon recycling, Matter **4**, 1391 (2021).

[46] T. Sham, R. Sammynaiken, Y. Zhu, P. Zhang, I. Coulthard, and S. Naftel, X-ray excited optical luminescence (XEOL): A potential tool for OELD studies, Thin Solid Films **363**, 318 (2000).

[47] G. Martínez-Criado, A. Homs, B. Alén, J. A. Sans, J. Segura-Ruiz, A. Molina-Sánchez, J. Susini, J. Yoo, and G.-C. Yi, Probing quantum confinement within single core–multishell nanowires, Nano Lett. **12**, 5829 (2012).

[48] G. Martínez-Criado, J. Villanova, R. Tucoulou, D. Salomon, J.-P. Suuronen, S. Labouré, C. Guilloud, V. Valls, R. Barrett, E. Gagliardini, *et al.*, ID16B: A hard x-ray nanoprobe beamline at the ESRF for nano-analysis, J. Synchrotron Radiat. **23**, 344 (2016).

[49] B.-H. Lin, Y.-H. Wu, X.-Y. Li, H.-C. Hsu, Y.-C. Chiu, C.-Y. Lee, B.-Y. Chen, G.-C. Yin, S.-C. Tseng, S.-H. Chang, *et al.*, Capabilities of time-resolved x-ray excited optical luminescence of the Taiwan Photon Source 23A x-ray nanoprobe beamline, J. Synchrotron Radiat. **27**, 217 (2020).

[50] M. E. Stuckelberger, T. Nietzold, B. M. West, Y. Luo, X. Li, J. Werner, B. Niesen, C. Ballif, V. Rose, D. P. Fenning, *et al.*, Effects of x-rays on perovskite solar cells, J. Phys. Chem. C **124**, 17949 (2020).

[51] J. Segura-Ruiz, D. Salomon, A. Rogalev, J. Eymery, B. Alén, and G. Martínez-Criado, Spatially and time-resolved carrier dynamics in core-shell InGaN/GaN multiple-quantum wells on GaN wire, Nano Lett. **21**, 9494 (2021).

[52] S. Levcenko, R. Biller, T. Pfeiffelmann, K. Ritter, H. H. H. H. Falk, T. Wang, S. Siebentritt, E. Welterb, and C. S. Schnohr, High-resolution XEOL spectroscopy setup at the x-ray absorption spectroscopy beamline P65 of PETRA III, J. Synchrotron Radiat. **29**, 1209 (2022).

[53] See the Supplemental Material at http://link.aps.org/supplemental/10.1103/PRXEnergy.3.023011 for elaborations on the experimental settings, J-V curves and laboratory-based evaluation of sister cells, elemental-distribution maps, wrinkle analysis, fitting parameters, and beam-damage considerations.

[54] V. Thomsen, Basic fundamental parameters in x-ray fluorescence, Spectroscopy **22**, 46 (2007).

[55] B. Henke, E. Gullikson, and J. Davis, X-ray interactions: Photoabsorption, scattering, transmission, and reflection at $E = 50$–$30\,000$ eV, $Z = 1$–92, At. Data Nucl. Data Tables **54**, 181 (1993).

[56] S. Ghosh, S. Mishra, and T. Singh, Antisolvents in perovskite solar cells: Importance, issues, and alternatives, Adv. Mater. Interfaces **7**, 2000950 (2020).

[57] J. Liu, M. De Bastiani, E. Aydin, G. T. Harrison, Y. Gao, R. R. Pradhan, M. K. Eswaran, M. Mandal, W. Yan, A. Seitkhan, *et al.*, Efficient and stable perovskite-silicon tandem solar cells through contact displacement by MgF_x, Science **377**, 302 (2022).

[58] M. C. Schubert, L. E. Mundt, D. Walter, A. Fell, and S. W. Glunz, Spatially resolved performance analysis for perovskite solar cells, Adv. Energy Mater. **10**, 1904001 (2020).

[59] K. Frohna, M. Anaya, S. Macpherson, J. Sung, T. A. S. Doherty, Y.-H. Chiang, A. J. Winchseter, K. W. P. Orr, J. E. Parker, P. D. Quinn, *et al.*, Nanoscale chemical heterogeneity dominates the optoelectronic response of alloyed perovskite solar cells, Nat. Nanotechnol. **17**, 190 (2022).

[60] Y. Wang, X. Quintana, J. Kim, X. Guan, L. Hu, C.-H. Lin, B. T. Jones, W. Chen, X. Wen, H. Gao, *et al.*, Phase segregation in inorganic mixed-halide perovskites: From phenomena to mechanisms, Photonics Res. **8**, A56 (2020).

[61] R. Chakraborty, J. Serdy, B. West, M. Stuckelberger, B. Lai, J. Maser, M. I. Bertoni, M. L. Culpepper, and T. Buonassisi, Development of an in situ temperature stage for synchrotron x-ray spectromicroscopy, Rev. Sci. Instrum. **86**, 113705 (2015).

[62] E. Aydin, J. Troughton, M. De Bastiani, E. Ugur, M. Sajjad, A. Alzahrani, M. Neophytou, U. Schwingenschlögl, F. Laquai, D. Baran, *et al.*, Room-temperature-sputtered nanocrystalline nickel oxide as hole transport layer for *p-i-n* perovskite solar cells, ACS Appl. Energy Mater. **1**, 6227 (2018).

[63] R. Azmi, E. Ugur, A. Seitkhan, F. Aljamaan, A. S. Subbiah, J. Liu, G. T. Harrison, M. Nugraha, M. K. Eswaran, M. Babics, *et al.*, Damp heat-stable perovskite solar cells with tailored-dimensionality 2D/3D heterojunctions, Science **376**, 73 (2022).

[64] F. Seiboth, F. Wittwer, M. Scholz, M. Kahnt, M. Seyrich, A. Schropp, U. Wagner, C. Rau, J. Garrevoet, G. Falkenberg, *et al.*, Nanofocusing with aberration-corrected rotationally parabolic refractive x-ray lenses, J. Synchrotron Radiat. **25**, 108 (2018).

[65] K. Suchan, Ph.D. dissertation, Lund University, 2023. https://lup.lub.lu.se/search/publication/6dcfcc33-b7b8-4cc1-942a-d70b483e4ed0.

[66] G. Vidon, P. Dally, M. Al-Katrib, D. Ory, M. Kim, E. Soret, E. Rangayen, M. Legrand, A. Blaizot, P. Schulz, *et al.*, The impact of x-ray radiation on chemical and optical properties of triple-cation lead halide perovskite: From the surface to the bulk, Adv. Funct. Mater. **33**, 2304730 (2023).

[67] A. García-Fernández, B. Kammlander, S. Riva, H. Rensmo, and U. B. Cappel, Composition dependence of x-ray stability and degradation mechanisms at lead halide perovskite single crystal surfaces, Phys. Chem. Chem. Phys. **26**, 1000 (2024).

[68] V. Solé, E. Papillon, M. Cotte, P. Walter, and J. Susini, A multiplatform code for the analysis of energy-dispersive x-ray fluorescence spectra, Spectrochim. Acta Part B **62**, 63 (2007).

[69] B. West, M. Stuckelberger, A. Jeffries, S. Gangam, B. Lai, B. Stripe, J. Maser, V. Rose, S. Vogt, and M. I. Bertoni, X-ray fluorescence at nanoscale resolution for multicomponent layered structures: A solar cell case study, J. Synchrotron Radiat. **24**, 288 (2017).

[70] E. V. Péan, S. Dimitrov, C. S. De Castro, and M. L. Davies, Interpreting time-resolved photoluminescence of perovskite materials, Phys. Chem. Chem. Phys. **22**, 28345 (2020).